A transformation approach for efficient evaluation of oscillatory surface integrals arising in three-dimensional boundary element methods

Article

Published Version

It is advisable to refer to the publisher's version if you intend to cite from the work. See Guidance on citing.

A transformation approach for efficient evaluation of oscillatory surface integrals arising in three-dimensional boundary element methods

Jonathan A. Hargreaves[1,*,†], Yiu W. Lam[1] and Stephen Langdon[2]

[1]*Acoustics Research Centre, Newton Building, University of Salford, Salford M5 4WT, UK*
[2]*Department of Mathematics and Statistics, University of Reading, Reading RG6 6AX, UK*

SUMMARY

We propose a method for efficient evaluation of surface integrals arising in boundary element methods for three-dimensional Helmholtz problems (with real positive wavenumber k), modelling wave scattering and/or radiation in homogeneous media. To reduce the number of degrees of freedom required when k is large, a common approach is to include in the approximation space oscillatory basis functions, with support extending across many wavelengths. A difficulty with this approach is that it leads to highly oscillatory surface integrals whose evaluation by standard quadrature would require at least $\mathrm{O}\left(k^2\right)$ quadrature points. Here, we use equivalent contour integrals developed for aperture scattering in optics to reduce this requirement to $\mathrm{O}\left(k\right)$, and possible extensions to reduce it further to $\mathrm{O}\left(1\right)$ are identified. The contour integral is derived for arbitrary shaped elements, but its application is limited to planar elements in many cases. In addition, the transform regularises the singularity in the surface integrand caused by the Green's function, including for the hyper-singular case under appropriate conditions. An open-source Matlab™code library is available to demonstrate our routines. © 2016 The Authors International Journal for Numerical Methods in Engineering Published by John Wiley & Sons Ltd.

1. INTRODUCTION

The boundary element method (BEM) can be an effective technique for simulating wave scattering and radiation problems in homogeneous media. Here, we consider scalar problems that can be modelled by the Helmholtz equation:

$$\nabla^2 \Phi + k^2 \Phi = 0, \tag{1}$$

where $k > 0$ is the wavenumber and Φ might for instance represent the pressure of an acoustic wave. By reformulating (1) as an integral equation that holds on the boundary of the medium, the dimensionality of the problem is reduced and unbounded homogeneous media can be modelled in a straightforward way.

Despite these advantages, standard BEM schemes using piecewise-polynomial basis functions have a computational cost that grows rapidly as the wavenumber k becomes large. This occurs because the boundary mesh must be refined to keep the elements small with respect to wavelength;

---

*Correspondence to: Jonathan A. Hargreaves, Acoustics Research Centre, Newton Building, University of Salford, Salford M5 4WT, UK.
†E-mail: j.a.hargreaves@salford.ac.uk

for a three-dimensional (3D) problem, with two-dimensional (2D) boundary, the number of elements, and therefore the number of degrees of freedom, must grow with $O(k^2)$ to maintain accuracy as k increases. BEM produces full interaction matrices linking every basis function to every other basis function, leading to excessive computational cost and storage requirements as k grows, even with application of fast multipole methods (e.g. [1]).

High frequency BEM (HF-BEM) approaches such as partition-of-unity BEM (POU-BEM) (e.g. [2]) and hybrid numerical asymptotic BEM (HNA-BEM) (e.g. [3]) aim to reduce storage requirements so as to make problems with larger k values tractable. The dominant strategy in these approaches is to replace the piecewise-polynomial basis functions with a smaller, ideally k-independent, number of appropriately chosen oscillatory basis functions, whose support may span many wavelengths. A consequence is that the computational cost of integrating each BEM matrix entry directly by quadrature, which is independent of k for standard BEM, scales for HF-BEM (in 3D) with $O(k^2)$ for collocation schemes and $O(k^4)$ for Galerkin schemes.

For HF-BEM algorithms to achieve their potential, there is therefore a need for algorithms that can efficiently evaluate the types of oscillatory integrals that arise. There has been significant progress towards achieving this for 2D HF-BEM schemes using Filon type methods (e.g. the recent review in Section 4 of [3]), but these ideas have yet to be fully extended to 3D scenarios. Ideas for computing the surface integrals that arise in 3D HF-BEM include those of Trevelyan and Honnor [4], and Bruno and Geuzaine [5]. The integration algorithm in [4] is based on element subdivision on a curvilinear grid, fitted such that the oscillation of the kernel occurs in one direction only. Integration in the direction perpendicular to the phase variation is performed using a standard Gauss-Legendre rule with a k-independent number of weights, leaving a set of one-dimensional (1D) oscillatory integrals that are evaluated with k-independent cost using the method of numerical steepest descent (e.g. [6]). The algorithm was shown to be capable of achieving near machine-precision with k-independent computational cost, but the algorithmic complexity involved meant this only outperformed standard approaches for quite large values of k. The algorithm in [5] is based on the observation that only the singular and stationary phase points contribute significantly to the value of oscillatory integrals, because the oscillation in other areas largely cancels out. The integrand may therefore be windowed in space to only include these regions, with the size of the windows reducing as k increases, but the asymptotic nature of the resulting scheme means it is not fully error controllable. Moreover, the construction of these window functions, in particular for the cases they may overlap, is an algorithmically complicated task; in [5], this scheme is only applied to the case of a spherical obstacle.

Here, we adopt an entirely different approach. Rather than examining the kernel of the surface integral and attempting to design algorithms to suit its characteristics (as was done in [3–5]), we instead use Stokes' theorem to transform the surface integral into a contour integral around its edge. This places some limitations on the geometry and the form of the integration kernels (Section 4), but results in a very simple algorithm, which is available in an accompanying Matlab toolbox (available to download from the publisher's website as the 'Supporting Information' that accompanies this manuscript).

Transformation of surface integrals to contour integrals is an approach that has been widely used in BEM, mainly to regularise the singularity present in the Green's function in cases where the evaluation point is adjacent to or on the element over which integration is being performed. The focus here has particularly been on integrals arising from the hyper-singular integral operator in collocation schemes (e.g. [7, 8]). An early and influential exposition of this approach was given by Terai [9], based on conversion to polar coordinates; this included support for higher-order polynomial basis functions, but was restricted to planar elements. More recently, there has been interest in evaluating the resulting line integrals analytically using a power series expansion [10], but this is valid only for piecewise-constant basis functions on planar polygonal elements.

The approach reported in this paper differs from those in [7, 10] in that it arises specifically from the wave nature of the fields involved. In particular, it draws on formulations derived for modelling aperture scattering, so has a specific physical interpretation. These integral transforms have been known for many decades, and some were specifically focussed on reducing computational cost of numerical integration (e.g. [11, 12]); however, their application to the computation

of BEM matrix coefficients is believed to be novel. One of the closest works to that contained herein is [13]; this treats a different class of oscillatory integral (a polynomial-exponential product), but does so by applying Stokes' theorem and identifies the same connection with aperture scattering problems.

The paper is structured as follows. In Sections 2.1 and 2.2, we review HF-BEM, and investigate the resulting wave behaviour. Following this, we describe an alternative grouping of discretisation terms and show how this more directly leads to a contour integral formulation. In Section 3, we review the aperture scattering formulations before discussing in Section 4 their application to integrals commonly found in HF-BEM, along with the contents of the Matlab toolbox.

2. BOUNDARY INTEGRAL EQUATION FORMULATION

2.1. The Kirchhoff-Helmholtz boundary integral equation

The Kirchhoff-Helmholtz boundary integral equation (KHBIE) is the foundation of the direct BEM. It is derived by applying Green's second identity to the free-space Green's function $G(\mathbf{x}, \mathbf{y}) = e^{ikR}/4\pi R$, where $R = |\mathbf{x} - \mathbf{y}|$, and a wave Φ, that is, a time-harmonic scalar field that satisfies the Helmholtz equation (1). Various configurations are possible, including 'interior problems' concerning a bounded medium in a cavity (Figure 1a) and 'exterior problems' concerning an obstacle submerged in an unbounded medium (Figure 1b). Excitation of the medium may come from part of the boundary (e.g. a vibrating panel) or from an additional incident wave pre-defined in the medium (a scattering problem). However, once all the necessary manipulations have been performed (e.g. using the Sommerfeld radiation condition to show that the contribution from the integral over S_∞ in Figure 1b is zero), then all these configurations result in very similar integral equations. Because our focus here is on evaluating integrals arising from the KHBIE rather than its various applications, it is convenient to state it abstractly without considering precisely which scenario it is being applied to. To this end, we define an operator $\mathcal{K}$, which maps a field Φ on a surface S to a field Ψ in the surrounding volume:

$$\Psi(\mathbf{x}) = \mathcal{K}\{\Phi\}(\mathbf{x}) = \iint\limits_S \hat{\mathbf{n}}(\mathbf{y}) \cdot [\Phi(\mathbf{y})\nabla G(\mathbf{x}, \mathbf{y}) - G(\mathbf{x}, \mathbf{y})\nabla\Phi(\mathbf{y})] dS_\mathbf{y}. \qquad (2)$$

Here, $\hat{\mathbf{n}}$ is the surface normal unit vector orientated into the acoustic medium, and ∇ is always taken with respect to $\mathbf{y}$ unless specifically stated otherwise (e.g. in Section 4.4). The surface-normal component of the gradient $\hat{\mathbf{n}} \cdot \nabla$ is often denoted by the shorthand $\partial/\partial n$, read as 'surface-normal derivative', and this will be used interchangeably in what follows. In scattering problems, Ψ equates
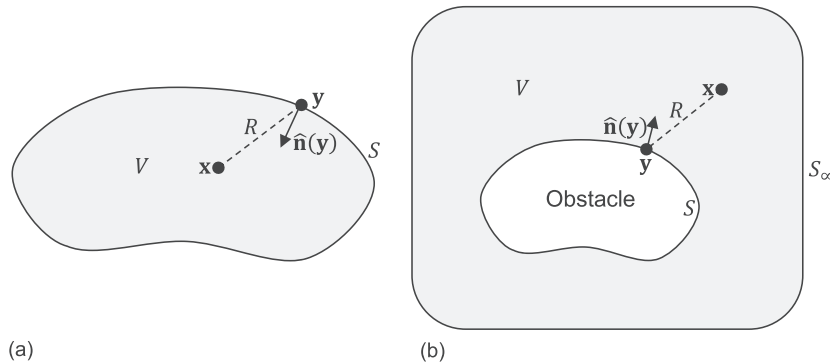
Figure 1. Geometries for the application of the Kirchhoff-Helmholtz boundary integral equation; (a) and (b) represent 'interior' and 'exterior' problems, respectively. In both cases, the volume V is connected and contains an acoustic medium. The boundary of V is the surface S in the interior case, or $S \cup S_\infty$ in the exterior case, and this has a normal vector $\hat{\mathbf{n}}$ orientated so as to point into V. Here, $\mathbf{y}$ is a point on S, and $\mathbf{x}$ is a point off S, and R denotes the distance between them.

to the scattered wave, that is, the total wave Φ minus the incident wave. Conversely in an interior problem (Figure 1a), where Φ is a known wave emanating from outside V, $\mathcal{K}$ acts as a 'reconstruction' operator, driving the monopole and dipole layers such that $\Psi(\mathbf{x}) = \Phi(\mathbf{x})$ if $\mathbf{x} \in V$. These two contrasting interpretations are emphasised because most POU-BEM and HNA-BEM implementations are focussed on scattering problems; the results of this paper are therefore most likely to be applied in that scenario, but the transforms described in Section 3 are motivated by the use of $\mathcal{K}$ to (partially) reconstruct a propagating wave.

This operator $\mathcal{K}$ is closely related to the classical single and double layer potentials S and D, which are the foundation of the indirect BEM:

$$S\{f\}(\mathbf{x}) = \iint_S G(\mathbf{x}, \mathbf{y}) f(\mathbf{y}) \, dS_{\mathbf{y}}, \tag{3}$$

$$D\{f\}(\mathbf{x}) = \iint_S \frac{\partial G}{\partial n}(\mathbf{x}, \mathbf{y}) f(\mathbf{y}) \, dS_{\mathbf{y}}. \tag{4}$$

The physical interpretation of S and D is as distributions on S of monopole and dipole sources, respectively; the surface quantity f is therefore interpreted as a source density function. Comparing (2) with (3) and (4), the operator $\mathcal{K}$ can be understood as layers of monopoles and dipoles working together, with densities specified by $-\partial\Phi/\partial n$ and Φ, respectively. Because G and $\partial G/\partial n$ both satisfy the Helmholtz equation for $\mathbf{x} \neq \mathbf{y}$, it follows that $\Psi(\mathbf{x})$ satisfies the Helmholtz equation for $\mathbf{x} \notin S$.

2.2. Discretisation

In order to permit numerical solution, the surface quantities Φ and $\partial\Phi/\partial n$ must be approximated in a discretised form, usually as weighted sums of basis functions $b_j(\mathbf{y})$:

$$\Phi(\mathbf{y}) \approx \sum_j w_j b_j(\mathbf{y}). \tag{5}$$

If an algorithm is being coded for a specific boundary condition, then it is often possible to eliminate Φ or $\partial\Phi/\partial n$ (e.g. for sound-hard or sound-soft obstacles) or to express one in terms of the other (e.g. for a locally-reacting surface impedance boundary condition). However in a multipurpose BEM code, it is more common to approximate Φ and $\partial\Phi/\partial n$ separately and then combine the results numerically using the boundary data supplied.

With HF-BEM, we attempt to reduce the number of degrees of freedom required to represent the oscillatory nature of Φ and $\partial\Phi/\partial n$ through intelligent design of the basis functions. A common form for b_j to take in these schemes is

$$b_j(\mathbf{y}) = e_j(\mathbf{y}) \mathbf{o}_j(\mathbf{y}). \tag{6}$$

Here, $\mathbf{o}_j$ is an oscillatory function, and e_j is an envelope function, usually both defined only on S. The purpose of $\mathbf{o}_j$ is to represent some aspect of the oscillatory behaviour present in Φ; plane waves are a common choice. The intention is that these will effectively represent the (often largely predictable) oscillation in Φ, leaving the 'envelope' functions e_j to interpolate a quantity that is slowly varying with respect to wavelength; piecewise-polynomials defined on a mesh of elements that are large with respect to wavelength are an effective choice for this. Because this scheme does not require the oscillations in Φ to be approximated by polynomials, it does not (in principle) require more degrees of freedom as k increases, provided appropriate choices of $\mathbf{o}_j$ are made.

2.3. Waves emanating from individual basis functions

We now consider the fields Ψ_j^S and Ψ_j^D arising from individual basis functions, where the superscript indicates the operator used and the subscript indicates that it has been applied to the jth basis function b_j. Specifically,

$$\Psi_j^S(\mathbf{x}) = S\{b_j\}(\mathbf{x}) = \iint\limits_{S_j} G(\mathbf{x}, \mathbf{y}) \, b_j(\mathbf{y}) \, dS_{\mathbf{y}}, \tag{7}$$

$$\Psi_j^D(\mathbf{x}) = D\{b_j\}(\mathbf{x}) = \iint\limits_{S_j} \frac{\partial G}{\partial n}(\mathbf{x}, \mathbf{y}) \, b_j(\mathbf{y}) \, dS_{\mathbf{y}}. \tag{8}$$

Here, $S_j = S \cap \sup(b_j)$ is the section of S on which b_j is non-zero. Clearly, from their definitions as integrals of G and $\partial G/\partial n$, respectively, both Ψ_j^S and Ψ_j^D satisfy the Helmholtz equation for $\mathbf{x} \notin S_j$. It is unusual to see Ψ_j^S and Ψ_j^D discussed in isolation; usually, they are only considered as a component of the total solution; however, it is actually the evaluation of Ψ_j^S and Ψ_j^D that dominates the assembly of the BEM linear system. The total field Ψ may also be recovered from a weighted sum of them, using the same weights that approximate Φ and $\partial\Phi/\partial n$ from the set of basis functions.

For standard BEM discretisation schemes, the behaviour of Ψ_j^S and Ψ_j^D is fairly predictable because these waves are dominated by the monopole and dipole behaviour of G and $\partial G/\partial n$. With a HF-BEM basis function of the form (6) however, the oscillatory behaviour of o_j will also influence the directivity of the resulting field, and the results become more interesting. Figure 2 shows slices through Ψ_j^S and Ψ_j^D for a square planar element S_j (with uniform normal vector $\hat{\mathbf{n}}_j$) on which the (plane wave) oscillatory basis function

$$o_j(\mathbf{y}) = e^{i\mathbf{k}_j \cdot [\mathbf{y} - \mathbf{v}_{\text{ref}}]} \tag{9}$$

is supported. Here, $\mathbf{v}_{\text{ref}} \in S_j$ is a fixed vertex (which provides a positional phase reference) and $\mathbf{k}_j$ is the wavevector of the plane wave; this points in the direction of propagation and has magnitude $|\mathbf{k}_j| = k$. The envelope function e_j was in this case chosen to be a piecewise-constant function:

$$e_j(\mathbf{y}) = \begin{cases} 1 & \text{if } \mathbf{y} \in S_j \\ 0 & \text{otherwise} \end{cases}. \tag{10}$$

The plots in Figure 2 are drawn in side view; the plane from which the points $\mathbf{x}$ were chosen passes through the centre of the element and is orientated to contain $\hat{\mathbf{n}}_j$ and $\mathbf{k}_j$. The element S_j is depicted by a heavy black line, and $\hat{\mathbf{n}}_j$ points vertically upwards. The wavenumber was chosen such that $ka = 40$, where a is the width of S_j.

The two plots are quite similar, although close to the plane of S_j there are some easily visible differences. In particular, the dipole radiation pattern of D means that the wave Ψ_j^D in Figure 2a

(a)   (b)
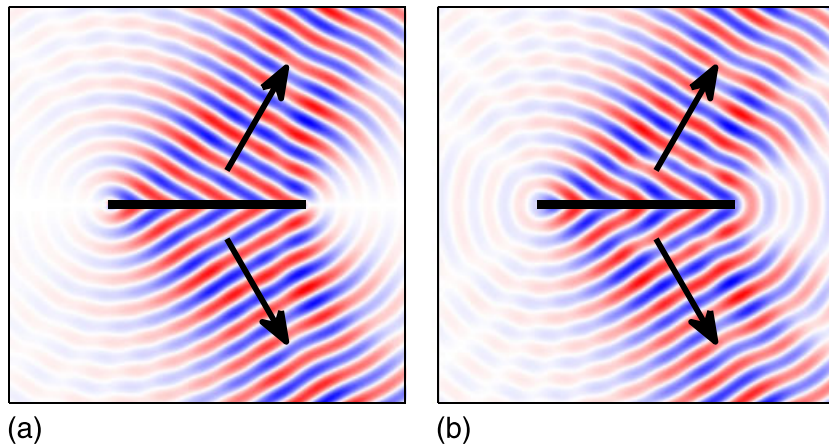
Figure 2. Plots versus observer position $\mathbf{x}$ of real part of the waves: (a) $\Psi_j^D(\mathbf{x})$ and (b) $\Psi_j^S(\mathbf{x})$. Red and blue indicate positive and negative values, respectively, and the arrows indicate the direction of propagation. Plots depict a slice through the wave in side view; the 'element' S_j is depicted by the heavy black line and the element normal vector $\hat{\mathbf{n}}_j$ points vertically upwards.

is anti-symmetric across the plane of S_j and most noticeably has opposite sign on each side of S_j and vanishes for $\mathbf{x}$ that are in the plane of S_j but not on S_j itself. Conversely, Ψ_j^S in Figure 2b is symmetric across the plane of S_j because of the monopole radiation pattern of S and does not vanish for $\mathbf{x}$ that are in the plane of S_j but not on S_j itself.

The arrows indicate the dominant directions of propagation; these are mirror images in the plane of S_j and are the same for both operators. These will be called the 'incoming' and 'outgoing' wave directions. These names refer to the fact that S_j, which is part of S, usually represents the boundary between an acoustic medium and an obstacle. The convention is that $\hat{\mathbf{n}}_j$ points into the medium; hence, for Figure 2 (in which $\hat{\mathbf{n}}_j$ points upwards), the medium is above the plane of S_j and the obstacle is below it. With this orientation, the 'incoming' direction is the downward arrow, arriving at the obstacle from the medium, and the upward arrow is the 'outgoing' direction, leaving the obstacle and propagating out into the medium. The corresponding wavevectors are respectively given by $\mathbf{k}_j^I = \mathbf{k}_j^t - \hat{\mathbf{n}}_j k_j^n$ and $\mathbf{k}_j^O = \mathbf{k}_j^t + \hat{\mathbf{n}}_j k_j^n$, where $\mathbf{k}_j^t$ is the surface tangential component of $\mathbf{k}_j$ and $k_j^n = \sqrt{k^2 - \left|\mathbf{k}_j^t\right|^2}$. Interestingly, this means that, for a planar surface element at least, the dominant directions in which Ψ_j^S and Ψ_j^D propagate out into V are independent of the surface normal component of the wavevector specified in (9). This is because it is the oscillation in o_j that specifies the dominant propagation directions, and for a planar surface element, this is purely controlled by $\mathbf{k}_j^t$; in its exponent, $\mathbf{k}_j \cdot [\mathbf{y} - \mathbf{v}_{\mathrm{ref}}] = \mathbf{k}_j^t \cdot [\mathbf{y} - \mathbf{v}_{\mathrm{ref}}]$ because $\mathbf{y}$ and $\mathbf{v}_{\mathrm{ref}}$ are coplanar, meaning $\hat{\mathbf{n}}_j \cdot [\mathbf{y} - \mathbf{v}_{\mathrm{ref}}] = 0$ and the value of k_j^n has no effect. In the examples in Figure 2, $\mathbf{k}_j^t$ points to the right of the figure and has magnitude $k/2$ (so $k_j^n = \sqrt{3}k/2$).

Because it is also required that $\left|\mathbf{k}_j\right| = k$, there are only two valid choices for $\mathbf{k}_j$ for a specified value of $\mathbf{k}_j^t$; $\mathbf{k}_j = \mathbf{k}_j^I$ and $\mathbf{k}_j = \mathbf{k}_j^O$. However, both of these choices produce identical results for Ψ_j^S and Ψ_j^D, and these in turn both show dominant propagation in directions $\mathbf{k}_j^I$ <u>and</u> $\mathbf{k}_j^O$ (as seen in Figure 2). These observations suggest that Ψ_j^S and Ψ_j^D may not be the most fundamental building blocks of what is emanating from b_j and that a scheme which emanates waves that propagate only in the directions $\mathbf{k}_j^I$ or $\mathbf{k}_j^O$ may be worth investigating.

2.4. An alternative approach to discretisation

Section 2.2 described the standard approach to discretisation of the single and double layer potential operators. Here, an alternative approach will be described, which substitutes basis functions directly into $\mathcal{K}$. This exploits the fact that, while the envelope function $e_j(\mathbf{y})$ is only defined for $\mathbf{y} \in S$, the oscillatory function $o_j(\mathbf{y})$ will in general be defined globally. Ultimately, the objective is to approximate Φ and $\partial\Phi/\partial n$ in a consistent way, which captures the leading order physical behaviour. Extending the idea that the wave behaviour should be captured by the oscillatory functions and that the envelope functions are primarily a partition-of-unity defined on the surface, an appropriate choice is to approximate $\partial\Phi/\partial n$ by

$$\frac{\partial\Phi}{\partial n}(\mathbf{y}) \approx \sum_j w_j e_j(\mathbf{y}) \frac{\partial o_j}{\partial n}(\mathbf{y}). \tag{11}$$

Comparing this to the approach in (8), the main change is that $\partial o_j / \partial n$ will now be used to capture the oscillation of $\partial\Phi/\partial n$, in place of o_j. This is justifiable because most common choices for o_j (ours in (9) included) are solutions of the Helmholtz equation themselves; hence, they are well suited to represent both Φ and $\partial\Phi/\partial n$ on S. In practice, for most likely choices of oscillatory function, $\partial o_j / \partial n$ is likely to have similar oscillatory behaviour to o_j, albeit with some scaling due to the presence of the differential, which may or may not be spatially dependent (e.g. the specific example in the following paragraph). Moreover, we are particularly interested in the possibility of using the same coefficient values w_j in both (5) and (11), so that Φ and $\partial\Phi/\partial n$ are approximated together, because this will be shown in Section 2.5 to be a prerequisite for application of Stokes' theorem. Considering this and the form of (11), it is therefore natural to consider the field arising

when a single basis function $b_j(\mathbf{y}) = e_j(\mathbf{y}) o_j(\mathbf{y})$ is substituted into both Φ and $\partial\Phi/\partial n$ within the KHBIE; we denote this field as $\Psi_j(\mathbf{x}) = \mathcal{K}\{b_j\}(\mathbf{x})$:

$$\Psi_j(\mathbf{x}) = \mathcal{K}\{b_j\}(\mathbf{x}) = \iint_{S_j} e_j(\mathbf{y})\,\hat{\mathbf{n}}(\mathbf{y}) \cdot \left[o_j(\mathbf{y})\,\nabla G(\mathbf{x},\mathbf{y}) - G(\mathbf{x},\mathbf{y})\,\nabla o_j(\mathbf{y})\right] dS_{\mathbf{y}}. \qquad (12)$$

We now go on to show that this form of discretisation scheme produces waves Ψ_j, which exhibit dominant propagation in only $\mathbf{k}_j^I$ or $\mathbf{k}_j^O$, as suggested in the previous section. Given that the KHBIE was derived from the assumption that the waves involved satisfied the Helmholtz equation, it makes sense now to only consider choices of o_j that satisfy this also. For planar elements and the plane wave basis defined in (9), this amounts to choosing $\mathbf{k}_j = \mathbf{k}_j^I$ or $\mathbf{k}_j = \mathbf{k}_j^O$ for a specified value of $\mathbf{k}_j^t$; this 'I' and 'O' superscript notion will be continued onto o_j, b_j and Ψ_j to indicate which choice of $\mathbf{k}_j^I$ or $\mathbf{k}_j^O$ has been used. This implies that the basis functions will naturally occur in pairs b_j^I and b_j^O, which have equal values of $\mathbf{k}_j^t$ and are equal on S_j, but which have opposite surface normal derivatives. Noting that $\partial o_j^I / \partial n(\mathbf{y}) = -i k_j^n o_j^I(\mathbf{y})$ and that $\partial o_j^O / \partial n(\mathbf{y}) = i k_j^n o_j^O(\mathbf{y})$, it follows that $\Psi_j^I(\mathbf{x}) = \mathcal{K}\{b_j^I\}(\mathbf{x}) = \Psi_j^D(\mathbf{x}) + i k_j^n \Psi_j^S(\mathbf{x})$ and $\Psi_j^O(\mathbf{x}) = \mathcal{K}\{b_j^O\}(\mathbf{x}) = \Psi_j^D(\mathbf{x}) - i k_j^n \Psi_j^S(\mathbf{x})$. These waves are shown in Figure 3 using the same parameters as Figure 2. It can be seen that Ψ_j^I and Ψ_j^O each possess only one dominant propagation direction; these are equal to $\mathbf{k}_j^I$ and $\mathbf{k}_j^O$, respectively.

A system of discretisation based on incoming and outgoing waves would require separate discretisation weights for b_j^I and b_j^O so the total number of degrees of freedom would be equal to a scheme based on D and S. Such a scheme would represent Φ on S as a weighted sum of wave terms o_j, albeit windowed by the envelope functions e_j. Particularly for asymptotically large k, where the propagation behaviour becomes geometric, it can be imagined that Ψ_j^I and Ψ_j^O are simpler components from which to construct the total solution off S, compared with Ψ_j^D and Ψ_j^S, which require addition or subtraction in order to represent a wave travelling in only one direction. Locally reacting impedance boundary conditions may also be readily incorporated. For example, if Φ and $\partial\Phi/\partial n$ on S_j are related by $\partial\Phi/\partial n = -i k \beta \Phi$, where β is the relative surface admittance, then it is straightforward to show that the weight of b_j^O should be R times the weight of b_j^I, where $R = \left(k_j^n - k\beta\right) / \left(k_j^n + k\beta\right)$ is the standard pressure reflection coefficient used in acoustics [14]. Initial studies into the pros and cons of discretising Φ and $\partial\Phi/\partial n$ together in this way are discussed in [15] and [16], and an equivalent method, which uses only surface normal wave directions (equivalent to $\mathbf{k}_j^t = \mathbf{0}$) on a mesh of elements which were small with respect to

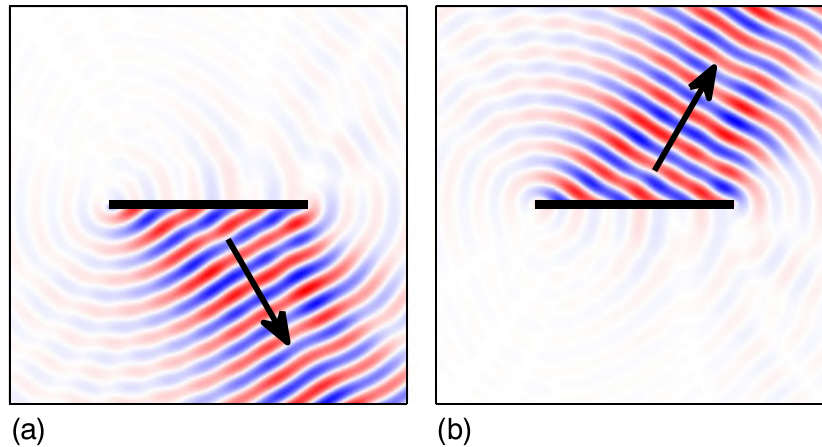(a)   (b)

Figure 3. Plots versus observer position $\mathbf{x}$ of real part of (a) the incoming wave $\Psi_j^I(\mathbf{x})$ and (b) the outgoing wave $\Psi_j^O(\mathbf{x})$. For other details, see Figure 2 caption.

wavelength, has been successfully applied in the time domain [17]. In the context of this paper however, this representation is used primarily as an intermediate step to permit fast evaluation of Ψ_j^D and Ψ_j^S.

2.5. Reduction of surface integral dimensionality

The integral in (12) to compute Ψ_j^I and Ψ_j^O has the same computational cost scaling as those to compute Ψ_j^D and Ψ_j^S; if a standard approach such as Gaussian quadrature is used, it will require $\mathrm{O}\left(k^2\right)$ operations to maintain accuracy as k grows. The strategy adopted here for reducing this is to transform each surface integral over S_j into a contour integral around the perimeter of S_j. So long as the integral kernels retain the same order of oscillatory behaviour then the reduction in dimensionality of the integrals (from surface integrals to line integrals) will reduce the computational cost scaling to $\mathrm{O}\left(k\right)$. The transformation of surface integrals into contour integrals in this paper amounts to application of Stokes' theorem, and this leads to a more concrete argument for evaluating Ψ_j^I and Ψ_j^O in preference to Ψ_j^D and Ψ_j^S.

Stokes' theorem for a vector field $\mathbf{J}$ may be stated as

$$\iint\limits_{S_j} \hat{\mathbf{n}}\left(\mathbf{y}\right)\cdot\nabla\times\mathbf{J}\left(\mathbf{y}\right)dS_{\mathbf{y}} = \oint\limits_{\partial S_j} \hat{\mathbf{l}}\left(\mathbf{y}\right)\cdot\mathbf{J}\left(\mathbf{y}\right)dl_{\mathbf{y}}. \qquad (13)$$

Here, $\hat{\mathbf{l}}$ is a unit vector tangential to the edge of the S_j, defined such that the contour integral around S_j and the normal vector $\hat{\mathbf{n}}$ obey the right-hand screw rule. Application to the KHBIE involves finding a choice for $\mathbf{J}$ such that $\hat{\mathbf{n}}\cdot\nabla\times\mathbf{J} = \hat{\mathbf{n}}\cdot\mathbf{I}$ on S_j, where $\mathbf{I}$ is the quantity to be integrated. Any choice for $\mathbf{J}$ must satisfy the divcurl identity $\nabla\cdot[\nabla\times\mathbf{J}]=0$, which implies that application of Stokes' theorem will only be directly possible for an $\mathbf{I}$ that satisfies $\nabla\cdot\mathbf{I}=0$.

If $e_j\left(\mathbf{y}\right)$ is taken to be piecewise-constant (as defined in (10)) then $\mathcal{K}\{b_j\}\left(\mathbf{x}\right)$ amounts to choosing $\mathbf{I}\left(\mathbf{x},\mathbf{y}\right) = o_j\left(\mathbf{y}\right)\nabla G\left(\mathbf{x},\mathbf{y}\right) - G\left(\mathbf{x},\mathbf{y}\right)\nabla o_j\left(\mathbf{y}\right)$; it is straightforward to show that the divergence of this equals zero if o_j and G satisfy the wave equation because the divergence of the two terms cancel (in the same way that they do in the derivation of the KHBIE using Greens' second identity). In contrast, choices for $\mathbf{I}$ corresponding to the operators D and S would each include only one of these terms; hence, the divergence is non zero and Stokes' theorem cannot be directly applied.

It therefore makes more sense to look for a contour integral transform for Ψ_j^I and Ψ_j^O. The main challenge here is to find an appropriate choice for $\mathbf{J}$, which matches with $\mathcal{K}\{b_j\}$; fortuitously, this is something that has already been addressed in classical optics. Most of those publications use differing notation and focus primarily on the case where the oscillatory function is a spherical wave; hence, a review is included in the next section. Reconstruction of Ψ_j^D and Ψ_j^S from Ψ_j^I and Ψ_j^O, including support for more realistic choices of envelope function, will then be addressed in Section 4.

3. FINDING A CONTOUR INTEGRAL KERNEL

The parallel problem, which has led to an appropriate formulation for $\mathbf{J}$, is the classical optics problem of calculating the field radiated through an aperture in an absorbing (optically black) screen. The starting point for this is a surface integral identical to (12), so long as e_j is defined to be piecewise-constant according to (10). In this analogy, o_j is regarded as being the incident wave arriving at the screen, S_j the aperture in the screen, and Ψ_j the wave emerging from it on the other side. It is widely known that this is an approximate model of aperture diffraction, but these approximations do not apply to our scheme because our interest is purely in calculating the field $\Psi_j\left(\mathbf{x}\right) = \mathcal{K}\{b_j\}\left(\mathbf{x}\right)$ emanating from one of our basis functions b_j. If we were to use such an HF-BEM algorithm to model diffraction from an aperture (e.g. [18]), then we would naturally include a set of multiple basis functions designed to capture all the possible (or likely) behaviour and represent the entire solution as a combination of these using weights found by a linear algebra

solver. Importantly, the transforms between surface and contour integrals discussed in the following sections are exact.

3.1. Maggi-Rubinowicz formulation

It is widely known that the Maggi-Rubinowicz formulation provides a means to transform this surface integral into a contour integral around the edge of the aperture. The mathematical representation of this was formalised by Miyamoto and Wolf in 1962 [19], which also contains a review of the earlier works on this topic. Here, it will be taken that o_j is the plane wave defined in (9), and it will be assumed that $|\mathbf{k}_j| = k$ in the medium, so o_j satisfies the Helmholtz equation. The known expression for Ψ_j corresponding to (12) is then [19]:

$$\Psi_j(\mathbf{x}) = \text{illum}_j(\mathbf{x})\, o_j(\mathbf{x}) + \oint_{\partial S_j} o_j(\mathbf{y})\, G(\mathbf{x}, \mathbf{y})\, \frac{\mathbf{k}_j \times \mathbf{R} \cdot \hat{\mathbf{l}}(\mathbf{y})}{kR - \mathbf{R} \cdot \mathbf{k}_j}\, dl_{\mathbf{y}}. \tag{14}$$

Here, $\mathbf{R} = \mathbf{x} - \mathbf{y}$, so $R = |\mathbf{R}| = |\mathbf{x} - \mathbf{y}|$ as previously defined. The kernel of the contour integral is a combination of the o_j at the edge point $\mathbf{y}$, multiplied by the Green's function from $\mathbf{y}$ to the observation point $\mathbf{x}$, multiplied by a directivity term. Note that there is no requirement for the aperture S_j to be planar; that was required in the previous section purely to allow reconstruction of Ψ_j^D and Ψ_j^S from Ψ_j^I and Ψ_j^O. This formulation therefore contains the same oscillatory terms as (12) but replaces the surface integral with a contour integral. Because of the reduced dimensionality, the numerical integration cost should therefore reduce from $O\left(k^2\right)$ for (12) to $O\left(k\right)$ for (14).

The first term on the right hand side of (14) is referred to as the geometric field in aperture diffraction problems; it is depicted in Figure 4a, being the oscillatory function o_j at the observation point $\mathbf{x}$ (note how it is now essential that o_j is defined through all of space) multiplied by a windowing function $\text{illum}_j(\mathbf{x})$. Mathematically, the reason for this additional term is that Stokes' theorem cannot be applied where $\mathbf{J}$ is singular, as the directivity function is at the point where the geometric propagation path passes through S_j (because $\mathbf{k}_j$ and $\mathbf{R}$ would point in the same direction hence $kR - \mathbf{R} \cdot \mathbf{k}_j = 0$). This point must therefore be excluded from the surface integral before Stokes' theorem is applied; Miyamoto and Wolf discuss this in more detail in Section 2 of [19] and show that it gives rise to the geometric field. The 'geometric region', in which $\text{illum}_j(\mathbf{x})$ is non-zero, is defined as any point $\mathbf{x}$ for which a line in the direction $-\mathbf{k}_j$ intersects S_j; this is straightforward
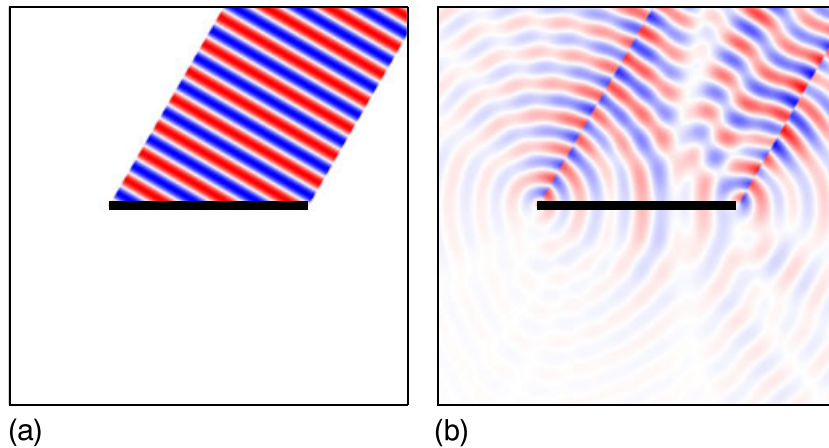

(a)   (b)

Figure 4. Decomposition of $\Psi_j^O(\mathbf{x})$ into two terms as used by the Maggi-Rubinowicz formulation: (a) the geometric term; (b) the result of the contour integral around the edge of S_j. The sum of these two terms is equal to $\Psi_j^O(\mathbf{x})$ as depicted in Figure 3b. For other details, see Figure 2 caption.

to compute if S_j is planar but can be more involved if S_j is curved. Note that the region is only projected forward from S_j with respect to $\mathbf{k}_j$, not backward; hence, there is still a discontinuity on S_j, which is consistent with the interpretation of it as containing a distribution of sources. A situation not typically considered in aperture problems but relevant to the BEM application herein is the case where $\hat{\mathbf{n}} \cdot \mathbf{k}_j < 0$. In this case, the illuminated region is still defined by S_j and $\mathbf{k}_j$ in the normal way, but the geometric scattered field now equals $-o_j(\mathbf{x})$ because of the anti-symmetry of (12) with respect to $\hat{\mathbf{n}}$. We incorporate this behaviour into $\mathrm{illum}_j(\mathbf{x})$ by defining it to equal $\mathrm{sign}\left(\hat{\mathbf{n}} \cdot \mathbf{k}_j\right)$ in the geometric region and zero otherwise.

Because the geometric component $\mathrm{illum}_j(\mathbf{x}) o_j(\mathbf{x})$ is discontinuous across the boundary of the geometric zone but the total field Ψ_j is not, it follows that the contour integral must give rise to a complementary discontinuity; this can be observed in Figure 4b. Mathematically, this occurs due to a zero in the numerator of the directivity term $\mathbf{k}_j \times \mathbf{R} \cdot \hat{\mathbf{l}}$, which has odd-symmetry in the plane of $\mathbf{k}_j \times \hat{\mathbf{l}}$, cancelling with the aforementioned singularity in the denominator. The presence of this discontinuity, however, causes difficulties for numerical integration algorithms; hence, the next section will examine an alternative formulation that is not affected by this issue.

The decomposition of Ψ_j in (14) and Figure 4, into a geometric term plus a correction, is also interesting from an asymptotic perspective because for very large k the geometric component is dominant, with the correction only being significant vanishingly close to the boundary of the geometric region in order to make the total field continuous. As $k \to \infty$, only the geometric component exists; this is the asymptotic form of Ψ_j. This indicates that in addition to thinking about the asymptotic form of the total solution Φ, as is often done in the design of HNA-BEM approximation spaces, one can also consider the asymptotic form of Ψ_j and therefore of the coefficients in the BEM interaction matrix. Indeed, it would be possible to compute the latter in $\mathrm{O}(1)$ time by only computing the geometric term of Ψ_j and setting the diffracted term to zero.

3.2. Asvestas' formulation

Asvestas published two papers in 1985 on the topic of converting aperture problems to contour integrals [11, 20]. In these he gave a formulation that circumvents the issue of the geometric visibility boundary singularity mentioned previously, plus a method for finding $\mathbf{J}$ for other choices of o_j. Unlike previous work where the statements for $\mathbf{J}$ were usually derived from some manner of geometric construction, Asvestas found $\mathbf{J}$ from $\mathbf{I}$ by a vector calculus identity. For this to be valid, a requirement is that o_j and G satisfy the wave equation (with respect to $\mathbf{y}$) everywhere, but this is not the case for G when $\mathbf{x} = \mathbf{y}$ so Asvestas first regularised $\mathbf{I}$ by subtracting $o_j(\mathbf{x}) \nabla_{\mathbf{y}} [1/4\pi R]$. In order to find the correct value for $\Psi_j(\mathbf{x})$, this regularising term must be added back in a second integral, and he shows this is equal to $o_j(\mathbf{x}) \Omega_{S_j}(\mathbf{x}) / 4\pi$, where $\Omega_{S_j}(\mathbf{x})$ is the solid angle subtended by the element S_j at point $\mathbf{x}$.

The same formulation is derived and explained in detail in Appendix A by considering a new geometric construction, created in such a way so as to eliminate the requirement for a regularising term. This involves replacing the surface section S_j with the outer surface of a truncated cone; this is depicted in Figure 5 and is defined as a cone with base equal to S_j and apex at $\mathbf{x}$, minus its
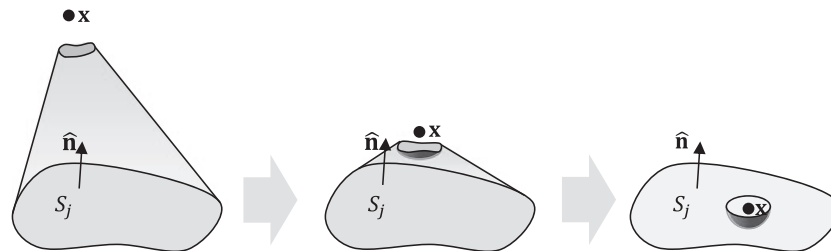

Figure 5. Truncated cone geometry for the derivation of Asvestas' formulation, showing that as $\mathbf{x}$ approaches S_j this becomes the standard geometry for evaluating the integral in the presence of the singularity in G.

intersection with a small sphere centred on $\mathbf{x}$. The total result, which is identical to (12) and (14), is as follows:

$$\Psi_j(\mathbf{x}) = \oint_{\partial S_j} \hat{\mathbf{n}}(\mathbf{y}) \cdot \mathbf{J}(\mathbf{x}, \mathbf{y}) \, dl_{\mathbf{y}} + \frac{\Omega_{S_j}(\mathbf{x})}{4\pi} o_j(\mathbf{x}). \tag{15}$$

Here, $\Omega_{S_j}(\mathbf{x})$ is the solid angle at $\mathbf{x}$ subtended by the surface section S_j. Note that orientation of $\hat{\mathbf{n}}$ with respect to $\mathbf{R}$ affects the sign of Ω_{S_j} (it is negative if $\mathbf{x}$ is below S_j with respect to $\hat{\mathbf{n}}$). It may also be computed by a contour integral around the edge of S_j [20]:

$$\Omega_{S_j}(\mathbf{x}) = -\oint_{\partial S_j} \frac{1}{R} \frac{\hat{\mathbf{z}} \times \mathbf{R} \cdot \hat{\mathbf{l}}(\mathbf{y})}{R + \hat{\mathbf{z}} \cdot \mathbf{R}} dl_{\mathbf{y}}. \tag{16}$$

Here, $\hat{\mathbf{z}}$ is a unit vector chosen such that the line extending from $\mathbf{x}$ in the direction $\hat{\mathbf{z}}$ does not intersect S_j; this is easily achieved by setting $\hat{\mathbf{z}}$ such that it points from the centre of S_j towards $\mathbf{x}$.

A particular advantage of this formulation is that $\mathbf{J}$ may be found for any choice of o_j that satisfies the Helmholtz equation by evaluating the integral ([11] and Appendix):

$$\mathbf{J}(\mathbf{x}, \mathbf{y}) = \int_0^R \frac{r}{R} \hat{\mathbf{R}} \times \mathbf{I}\left(\mathbf{x}, \mathbf{x} - r\hat{\mathbf{R}}\right) dr. \tag{17}$$

Here, $\hat{\mathbf{R}} = \mathbf{R}/R$ is a unit vector pointing from $\mathbf{y}$ on ∂S_j to $\mathbf{x}$. For the case where o_j is a plane wave defined by (9), this gives

$$\begin{aligned}
\mathbf{J}(\mathbf{x}, \mathbf{y}) &= -o_j(\mathbf{x}) \frac{\hat{\mathbf{R}} \times i\mathbf{k}_j}{4\pi R} \int_0^R e^{ir[k - \mathbf{k}_j \cdot \hat{\mathbf{R}}]} dr \\
&= -o_j(\mathbf{x}) \frac{\mathbf{R} \times \mathbf{k}_j}{4\pi R} \frac{e^{i[kR - \mathbf{k}_j \cdot \mathbf{R}]} - 1}{kR - \mathbf{k}_j \cdot \mathbf{R}} \\
&= o_j(\mathbf{x}) \frac{\mathbf{k}_j \times \mathbf{R}}{4\pi R} i e^{i[kR - \mathbf{R} \cdot \mathbf{k}_j]/2} \mathrm{sinc}\left(\frac{kR - \mathbf{R} \cdot \mathbf{k}_j}{2}\right).
\end{aligned} \tag{18}$$

Expressing the later term as a sinc function is advantageous numerically, because the result where $kR - \mathbf{k}_j \cdot \mathbf{R}$ tends to zero is well defined, meaning $\mathbf{J}$ is well behaved across the geometric visibility boundary. The solid angle term is of course independent of $\mathbf{k}_j$, meaning that the formulation in (15) is devoid of issues across the geometric visibility boundary and is therefore numerically favourable compared with (14). It is interesting to note that it was the solid angle $\Omega_{S_j}(\mathbf{x})$ that was removed to give this numerically-robust edge kernel, because that is also what is subtracted in many regularisation schemes for the hyper-singular operator (e.g. [7, 8]].

3.3. The case where $\mathbf{x}$ approaches $\mathbf{S}$

An important case that has been ignored in what has been written so far is the one when $\mathbf{x}$ approaches S. Evaluating such integrals correctly is paramount for BEM, because they arise in the extremely critical 'self-interaction' coefficients and the singularity in $\partial G/\partial n$ defeats standard numerical quadrature methods. Indeed, most of the contour integral transforms published in the BEM literature are solely focussed on this case (e.g. [7–9]).

It is widely known that the correct way to evaluate this is to deform the surface close to $\mathbf{x}$ such that $\mathbf{x}$ remains strictly within V. The most convenient geometry for this is to subtract a small disk of radius ϵ centred on $\mathbf{x}$ from S and to then replace it with a hemisphere of equal position and dimensions orientated away from V (see the right-most graphic in Figure 5). It can be shown that when ϵ tends to zero the surface integral over the hemisphere contributes $\Phi(\mathbf{x})/2$, so long as $\mathbf{x}$ is

on a smooth part of S (e.g. [21, 22]), and this is usually brought outside the surface integral as an explicit term. The remaining surface integral excludes the disk around $\mathbf{x}$, so as ϵ tends to zero this has the form of a 'Cauchy Principal Value' integral, often indicated by a horizontal line through the integral sign. Guiggiani has however pointed out [21, 22] that this is merely a notational convenience and that any modification to S that puts $\mathbf{x}$ definitively on one side of it or the other is permissible (pre-empting in a sense the modification to S which is proposed herein).

In this work however, the use of such notation has been resisted and the surface integrals have been written in a straightforward way. The motivation for this is the observation illustrated in Figure 5, that as $\mathbf{x}$ approaches S_j, the geometry that leads to Asvestas' formulation flattens to become the accepted geometry for evaluation of self-interaction. Thus, self-interaction is no-longer a special case and the problem singularity is regularised automatically by the contour integral transform. Indeed, the only special consideration that must be implemented is to force $\hat{\mathbf{z}} = \hat{\mathbf{n}}$ to match the convention that $\hat{\mathbf{z}}$ is chosen such that it points from S_j to $\mathbf{x}$.

3.4. Albani's Incremental Geometrical Optics formulation

Albani also addressed the issue of the singularity in the kernel of the contour integral of (14) in 2011 [23]. His formulation is derived in a similar manner to the Maggi-Rubinowicz statements, but he then goes on to express the geometric visibility function $illum_j(\mathbf{x})$ as a contour integral; he calls this the Incremental Geometrical Optics term. He goes on to show that part of this may be combined with the edge diffraction contour integral kernel, leading to exactly the same expression that appears in 3.3. His formulation is therefore also well behaved across the visibility boundary.

There are no particular numerical advantages of the Albani formulation compared with that of Asvestas. An important contribution it does make however is that it shows how the Maggi-Rubinowicz form in Section 3.1 and that of Asvestas in Section 3.2 are equivalent. In particular, the Albani formulation can be shown to be a special case of the Asvestas version with a particular choice of $\hat{\mathbf{z}}$. Albani states this himself for spherical incident waves; for an incident plane wave the equivalence is as follows. If $\mathbf{x}$ lies behind the aperture (with respect to the arriving wave), so $\mathbf{R} \cdot \mathbf{k}_j$ is predominately positive, then Albani's extra term is equivalent to (16) with $\hat{\mathbf{z}} = \mathbf{k}_j$. Alternatively, if $\mathbf{x}$ lies in front of the aperture, so $\mathbf{R} \cdot \mathbf{k}_j$ is predominately negative, then Albani's extra term is equivalent to (16) with $\hat{\mathbf{z}} = -\mathbf{k}_j$. Both choices are essentially used to compute $\Omega_{S_j}(\mathbf{x})$.

This equivalence is touched on more in the appendix. For now it is useful to know that the formulations in Sections 3.1 and 3.2 are equivalent; because they each have advantages in different situations and they are both in the toolbox.

4. APPLICATION TO COMPUTING HIGH FREQUENCY BOUNDARY ELEMENT METHOD INTEGRALS

The previous section described efficient methods to compute $\Psi_j(\mathbf{x}) = \mathcal{K}\{b_j\}(\mathbf{x})$, as given in (12) with e_j chosen to be piecewise-constant as defined in (10), but this is not a quantity that existing HF-BEM algorithms regularly compute. Instead, it is usually the terms Ψ_j^S and Ψ_j^D that are of interest, so this section will first examine the computation of those. How to apply these methods to more typical choices of e_j will then be discussed.

4.1. Computing Ψ_j^D and Ψ_j^S from Ψ_j^I and Ψ_j^O

The equivalences between Ψ_j^D and Ψ_j^S and Ψ_j^I and Ψ_j^O were given in Section 2.4 as $\Psi_j^I(\mathbf{x}) = \Psi_j^D(\mathbf{x}) + ik_j^n\Psi_j^S(\mathbf{x})$ and $\Psi_j^O(\mathbf{x}) = \Psi_j^D(\mathbf{x}) - ik_j^n\Psi_j^S(\mathbf{x})$. These relations require that the surface section S_j is planar. Note that this is not a requirement for the contour integration methods given in Section 3 to compute Ψ_j^I and Ψ_j^O; they can also be applied to curved surfaces. Statements to compute Ψ_j^D and Ψ_j^S are readily found by the sum and difference of these:

$$\Psi_j^D(\mathbf{x}) = D\{b_j\}(\mathbf{x}) = \frac{1}{2}\left[\mathcal{K}\{b_j^I\}(\mathbf{x}) + \mathcal{K}\{b_j^O\}(\mathbf{x})\right] = \frac{1}{2}\left[\Psi_j^I(\mathbf{x}) + \Psi_j^O(\mathbf{x})\right], \quad (19)$$

$$\Psi_j^S(\mathbf{x}) = S\{b_j\}(\mathbf{x}) = \left[\mathcal{K}\{b_j^{\mathrm{I}}\}(\mathbf{x}) - \mathcal{K}\{b_j^{\mathrm{O}}\}(\mathbf{x})\right]/2ik_j^n = \left[\Psi_j^{\mathrm{I}}(\mathbf{x}) - \Psi_j^{\mathrm{O}}(\mathbf{x})\right]/2ik_j^n. \quad (20)$$

Computing Ψ_j^D by (19) is straightforward. The formula for Ψ_j^S in 4.2 is, however, undefined for basis functions corresponding to plane waves that are surface tangential (i.e. $\left|\mathbf{k}_j^t\right| = k$) and is ill-conditioned when they are close to tangential ($\left|\mathbf{k}_j^t\right| \cong k$). Numerically, this is because in those cases $k_j^n \approx 0$ and $b_j^{\mathrm{I}} \approx b_j^{\mathrm{O}}$; hence, both the numerator and the denominator tend to zero. Physically, this corresponds to the property that a pressure-release surface, as S alone represents, does not support surface tangential plane waves, because the boundary condition $\Phi = 0$ forces their amplitudes to be zero. Conversely, D represents a rigid plane, and this can support surface tangential plane waves because they satisfy $\partial\Phi/\partial n = 0$ for any amplitude; hence, it is unsurprising that computing $D\{b_j\}$ for $\left|\mathbf{k}_j^t\right| = k$ is not a problem.

A possibility not yet considered is that the surface tangential wavenumber $\left|\mathbf{k}_j^t\right|$ may be greater than k in the medium. This corresponds to a plane wave, which is evanescent, or inhomogeneous in Miyamoto and Wolf's terminology, and manifests as k_j^n being imaginary. This is considered in Section 3.2 of [19] where it is shown that the geometric term exists only in the plane of the element. This would bring various complications in terms of having the geometric visibility boundary (where the Maggi-Rubinowicz contour integral kernel is singular) located in the plane of the element, thereby causing big problems for self-interaction calculations. However, it turns out that Asvestas' formulation in Section 3.2 can be applied directly without issue. The only issue is that the magnitude of $o_j(\mathbf{x})$ may become very large when $\mathbf{x}$ is far away from the plane of S_j; in principle, this is counteracted by the solid angle term in (15) cancelling with the contour integral kernel, but in practice it leads to significant subtraction error when used with numerical quadrature. In this case, away from the problematic geometric zone, it is better to switch to the edge diffraction formulation in Section 3.1, for which in this case no geometric term is required. The results of these computations are shown in Figure 6. For Ψ_j^{I} and Ψ_j^{O}, it can be seen that the strongest radiation occurs just below and just above the element, respectively, whereas for Ψ_j^D and Ψ_j^S, the field is anti-symmetric and symmetric, respectively; all these characteristics match what would be expected from Figure 2 and Figure 3. Interestingly, it can also be observed that for Ψ_j^{I} and Ψ_j^{O}, the wavelength appears to differ on each side of the element. This makes sense because one side is driven with $\left|\mathbf{k}_j^t\right| > k$ whereas the other side is not driven and waves propagate normally with wavenumber k.

A final comment is to observe the equivalence between the approach described previously, particularly the variant in Section 3.1 that uses a geometric term plus edge diffraction, and the widely used contour integral expressions for computing self-interaction on piecewise-constant basis functions on planar elements (e.g. in [9]). This amounts to taking $\mathbf{k}_j = \pm k\hat{\mathbf{n}}$, in which case $\mathbf{k}_j^t = \mathbf{0}$ and the basis functions are constant over the surface element. This was demonstrated in [17], where pairs
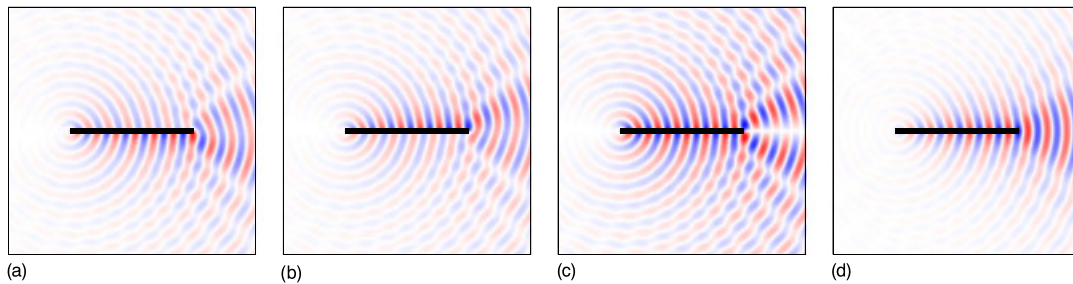

(a)   (b)   (c)   (d)

Figure 6. Plots versus observer position $\mathbf{x}$ of real part of (a) $\Psi_j^{\mathrm{I}}(\mathbf{x})$, (b) $\Psi_j^{\mathrm{O}}(\mathbf{x})$, (c) $\Psi_j^D(\mathbf{x})$ and (d) $\Psi_j^S(\mathbf{x})$. These are plotted for $\left|\mathbf{k}_j^t\right| = 1.02k$, so the basis function is a rightwards propagating plane wave that is slightly evanescent. For other details, see Figure 2 caption.

of incoming and outgoing surface-normal plane waves were used in a time domain BEM scheme with the integrals therein evaluated as equivalent contour integrals.

4.2. Numerical results for piecewise-constant $\mathbf{e}_j$

The numerical integration algorithm outlined earlier is implemented in the Matlab™toolbox, which accompanies this publication. This requires the elements S_j to be planar polygons, defined as a collection of N_j co-planar vertices $\mathbf{v}_i$, for $1 \leq i \leq N_j$, connected by edges $\mathbf{l}_i = \mathbf{v}_{(i \bmod N_j)+1} - \mathbf{v}_i$. In all cases, the reference vertex $\mathbf{v}_{\text{ref}}$ in the definition of o_j in (9) was taken to equal $\mathbf{v}_1$.

The integrals are performed using Matlab's built-in adaptive integration routines; these are not computationally fast but are effective to demonstrate that the implementations are correct and that the computational cost scaling occurs in the expected way. In addition to the scheme described earlier, the surface integral definitions of Ψ_j^D, Ψ_j^S, Ψ_j^I and Ψ_j^O were also implemented directly using adaptive 2D integration for use as a reference method. Both integration routines were run with the default accuracy tolerances, an absolute error magnitude of 10^{-10} and a relative error magnitude of 10^{-6}. For more information on these criteria, see the Matlab documentation.

Verification for the case where $\mathbf{x} \notin S_j$ was straightforward. This involved a large number of randomly generated configurations comprising all possible combinations of eight randomly generated elements of unit area, four polygonal and four parallelogram; 10 randomly generated locations for $\mathbf{x}$, all within distance 2 of S_j; 10 randomly generated values for $\mathbf{k}_j^t / k$ (i.e. basis function wave directions), some of which were evanescent. These were then all computed for all variants of Ψ_j at 21 logarithmically spaced values of k between $k = 10$ and $k = 100$ rad/m. Error between the contour scheme and the reference scheme was less than 10^{-8} in all cases.

A similar setup was used to assess the computational complexity. For this, code was inserted into the integration kernels to count the number of evaluation abscissae the adaptive schemes required to satisfy their error criterion. The testing methodology here was the same but a slightly smaller number of element shapes and values for $\mathbf{k}_j^t / k$ were used; 6 and 5, respectively. In addition, it was necessary to run the contour scheme at a higher range of k in order to see the computational cost trend clearly; these values were logarithmically spaced between $k = 100$ and $k = 10,000$ rad/m. Results are shown in Figure 7 for all four variants of Ψ_j; each line is the number of evaluation abscissae used to adequately calculate one of these operators for one combination of S_j, $\mathbf{x}$ and $\mathbf{k}_j^t / k$, plotted versus k. Figure 7a shows results from the contour integration scheme, Figure 7b from the direct implementation of the surface integral. Overlaid are the upper bounds in computational complexity expected from the integral dimensionality. It can clearly be seen that the contour scheme in Figure 7a
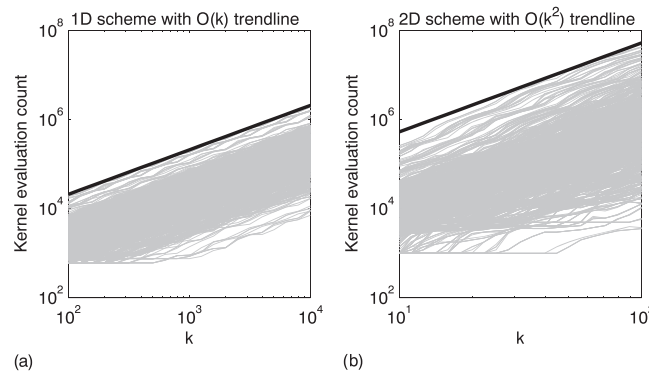

(a) (b)

Figure 7. Computational cost trends for evaluation of Ψ_j using (a) the 1D contour integral implementation; (b) a direct 2D integral implantation. Plots show the number of kernel evaluations required by an adaptive integration routine to meet a given error threshold. Overlaid are the expected upper bounds expected from the integral dimensionality. Note that the range of k used for the two implementations differed, because of the excessive cost of the 2D scheme for large k.

requires O (k) kernel evaluations, whereas the direct evaluation of the surface integral in Figure 7b requires at least O (k^2).

Verification for $\mathbf{x} \in S_j$ was more involved; this case causes no trouble for the contour scheme, but the direct implementation of the surface integral is unable to handle the singularity in G. To compute a reference result, an alternate algorithm had to be implemented. In this, the integration surface was modified to take advantage of the fact that, because of Green's second identity, the values of Ψ_j^I and Ψ_j^O will be identical when computed over any surface with the same edge as S_j, so long as $\hat{\mathbf{n}} \cdot \mathbf{R}$ is positive everywhere on it; this is the same idea used in the alternative definition of Asvestas' formulation given in the appendix. The polygon S_j was therefore replaced by the outer surface of a pyramid with S_j as its base and its apex slightly below $\mathbf{x}$ (with respect to $\hat{\mathbf{n}}$). Ψ_j^I and Ψ_j^O were computed over this and Ψ_j^D and Ψ_j^S were found from them using (19) and (20). Error between the contour scheme and the reference scheme was less than 10^{-8} for most cases, with a few evanescent basis functions giving marginally larger errors less than 10^{-6}. The source of these larger errors was, however, the reference scheme, not the contour scheme under test. They arise due to multiplication of the numerical integration result by the value of o_j at the pyramid apex, because this can have magnitude greater than one for outgoing evanescent waves.

4.3. Application with trigonometric partition-of-unity envelope functions

So far only piecewise-constant envelope functions have been considered, but these are not commonly used in POU-BEM because they do not satisfy Melenk and Babuška's smoothness conditions [24]. Instead, it is most common to borrow the Lagrangian quadratic shape functions used in standard BEM. It is however unclear how the integration algorithm given earlier could be applied for polynomial functions of quadratic order and above (for an outline of a possible extension to handle linear envelope functions, see the further research proposed in Section 5).

In [25], Peake *et al.* defined a set of trigonometric POU envelope functions as an alternative to the standard Lagrangian quadratic shape functions. This was motivated by the observation that error in POU-BEM schemes is often largest around the ends of elements where the transition between standard quadratic shape functions defined on different elements is not smooth, even if they are given the same nodal coefficient to enforce continuity. In contrast, the new envelope functions of Peake *et al.* all possess zero gradient at the limits of their support; when joined, they create a smooth envelope. In [25], they are defined for the local coordinate range $-1 \leq \mu \leq 1$, but in this paper, the range $0 \leq \mu \leq 1$ is used; for this they scale to become

$$N_1(\mu) = \frac{1}{4} + \frac{1}{4}\cos(2\pi\mu) + \frac{1}{2}\cos(\pi\mu),$$

$$N_2(\mu) = \frac{1}{2} - \frac{1}{2}\cos(2\pi\mu), \tag{21}$$

$$N_3(\mu) = \frac{1}{4} + \frac{1}{4}\cos(2\pi\mu) - \frac{1}{2}\cos(\pi\mu).$$

N_1, N_2 and N_3 are shown in Figure 8. For a quadrilateral element, they may be combined with the oscillatory function by tensor product, for example, $b_{j,l,m}(\mathbf{y}(\mu_1, \mu_2)) = \mathrm{o}_j(\mathbf{y}(\mu_1, \mu_2)) N_l(\mu_1) N_m(\mu_2)$.

The suitability of these functions for integration using the method developed earlier stems from the fact that they are weighted sums of trigonometric functions, which themselves may be expressed as combinations of oscillatory functions. For example, using $\cos\theta = \left[e^{i\theta} + e^{-i\theta}\right]/2$ gives $N_1(\mu) = \frac{1}{8}e^{i2\pi\mu} + \frac{1}{4}e^{i\pi\mu} + \frac{1}{4}e^{i0\pi\mu} + \frac{1}{4}e^{-i\pi\mu} + \frac{1}{4}e^{-i2\pi\mu}$. Each of these terms may be integrated separately, meaning that for a quadrilateral element, the results for the nine possible combinations of trigonometric envelope functions may be found by various weighted combinations of results for 25 oscillatory envelope functions. Moreover, if the element is a parallelogram, so $\mathbf{y}(\mu_1, \mu_2) = \mathbf{v}_1 + \mu_1\mathbf{l}_1 + \mu_2\mathbf{l}_2$ then this additional oscillation may be incorporated into $\mathbf{k}_j^t$. For example, if o_j is multiplied by two other oscillatory functions $e^{ic_1\mu_1}$ and $e^{ic_2\mu_2}$, then it can be shown
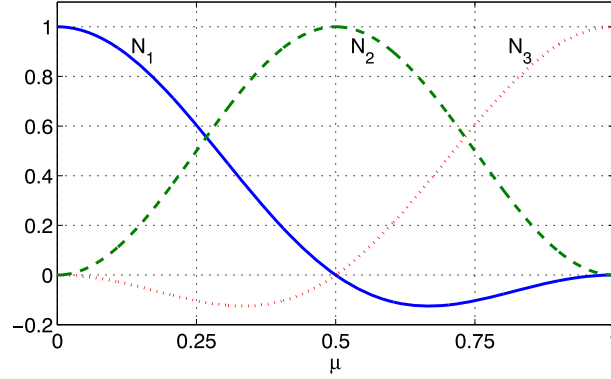
Figure 8. The trigonometric partition-of-unity envelope functions of Peake *et al.* scaled to the range $0 \leq \mu \leq 1$.
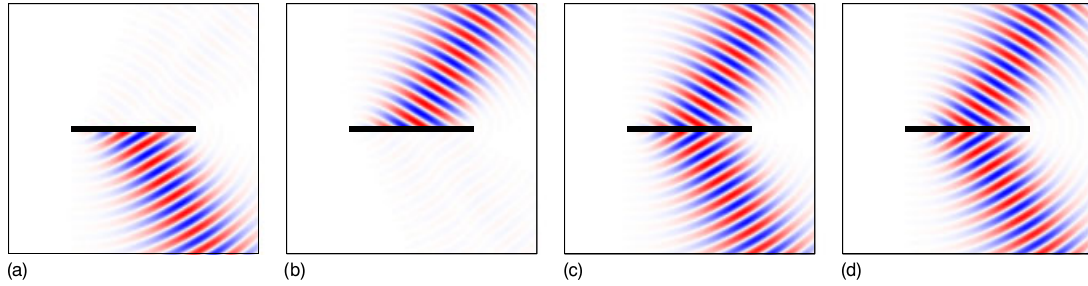

(a)　　　　(b)　　　　(c)　　　　(d)

Figure 9. Plots versus observer position $\mathbf{x}$ of real part of (a) $\Psi_j^I(\mathbf{x})$, (b) $\Psi_j^O(\mathbf{x})$, (c) $\Psi_j^D(\mathbf{x})$ and (d) $\Psi_j^S(\mathbf{x})$. These are computed for an envelope function equal to the product of the N_2 function of Peake *et al.* applied in both local coordinate directions. For other details, see Figure 2 caption.

that $\mathrm{o}_j\left(\mathbf{y}\left(\mu_1, \mu_2\right)\right) e^{ic_1\mu_1} e^{ic_2\mu_2} = e^{i\mathbf{k}_j^t \cdot [\mathbf{y}(\mu_1,\mu_2)-\mathbf{v}_1]} e^{ic_1\mu_1} e^{ic_2\mu_2} = e^{i\left[\mathbf{k}_j^t + c_1\tilde{\mathbf{k}}_1 + c_2\tilde{\mathbf{k}}_2\right] \cdot [\mathbf{y}(\mu_1,\mu_2)-\mathbf{v}_1]}$, where $\tilde{\mathbf{k}}_1 = \left[|\mathbf{l}_2|^2 \mathbf{l}_1 - (\mathbf{l}_1 \cdot \mathbf{l}_2) \mathbf{l}_2\right] \big/ |\mathbf{l}_1 \times \mathbf{l}_2|^2$ and $\tilde{\mathbf{k}}_2 = \left[|\mathbf{l}_1|^2 \mathbf{l}_2 - (\mathbf{l}_1 \cdot \mathbf{l}_2) \mathbf{l}_1\right] \big/ |\mathbf{l}_1 \times \mathbf{l}_2|^2$. Note that this approach of changing $\mathbf{k}_j^t$ only works directly for Ψ_j^D and Ψ_j^S because it affects $\partial b_j / \partial n$ in unintended ways when computing $\mathcal{K}\{b_j\}(\mathbf{x})$. Ψ_j^I and Ψ_j^O with the envelope functions of Peake *et al.* may, however, be found from windowed results for Ψ_j^D and Ψ_j^S if required.

This approach is implemented in the accompanying Matlab toolbox by calling the integration functions for piecewise-constant envelopes as a subroutine and combining the results. Verification for the case where $\mathbf{x} \notin S_j$ was performed in exactly the same manner as in the previous section and error between the two algorithms was below 10^{-8} in all cases. Verification was not performed for the case where $\mathbf{x} \in S_j$ because this would lead to an extremely complicated reference algorithm. However, because the subroutines are already verified for this case and their combination has been verified by the $\mathbf{x} \notin S_j$ result, we can deduce that the new routines for the envelope functions of Peake *et al.* will work in the $\mathbf{x} \in S_j$ case too. The computation cost scaling of these routines is directly inherited from the result in Figure 7 by the same reasoning.

Plots of all four variants of Ψ_j computed with a POU envelope function are shown in Figure 9. In this, the envelope function chosen was the product of the N_2 function of Peake *et al.* applied in both local coordinate directions. The profile of the envelope function can be clearly seen in the emanated field Ψ_j, although it appears to become wider with increasing distance from S_j. Compared with Figures 2 and 3, a key difference is that the tapering of the envelope function towards the edges of the element has significantly reduced the diffraction effects. This has interesting implications as k becomes asymptotically large. The geometric approximation to Ψ_j^O is shown in Figure 10a; this
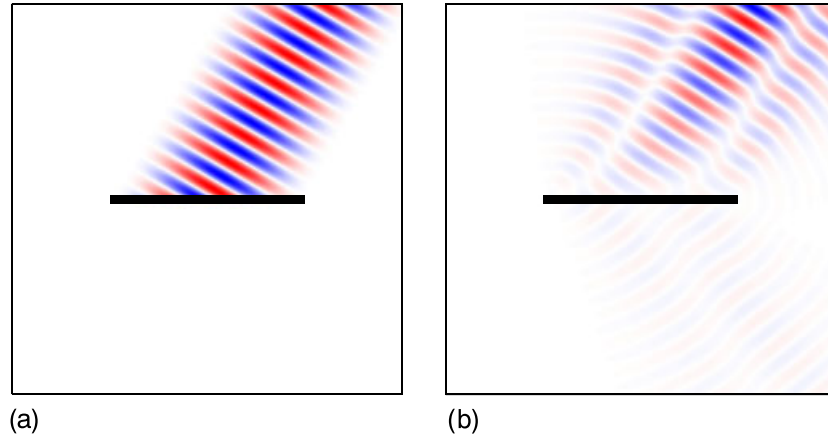
(a)   (b)

Figure 10. Decomposition of $\Psi_j^O(\mathbf{x})$ into two terms when an envelope function equal to the product of the N_2 function Peake *et al.* in both local coordinate directions has been applied: (a) the geometric term; (b) the result of the contour integral around the edge of S_j. The sum of these two terms is equal to $\Psi_j^O(\mathbf{x})$ as depicted in Figure 9b. For other details, see Figure 2 caption.

is simply the oscillatory function $o_j(\mathbf{x})$ multiplied by the envelope function projected out in the direction $\mathbf{k}_j^O$ (in the same manner that projecting a piecewise-constant envelope function produces $\text{illum}_j(\mathbf{x})$ in (14)). The remaining diffracted component is shown in Figure 10a. This was computed by subtracting the geometric approximation in Figure 10a from the exact result in Figure 9b; unfortunately, no closed form expression for it is available. The result is, however, interesting because there is little effect near S_j because the envelope function eliminates the diffraction effects. The strength of the field further away is required to express the spreading of the beam with distance. In terms of partial differential equations, this difference can be explained by the fact that the geometric approximation to Ψ_j^O in Figure 10a satisfies the paraxial approximation to the Helmholtz equation, whereas the field in Figure 9b satisfies the Helmholtz equation proper.

4.4. Computing the gradient of Ψ_j

Many BEM formulations use not only S and D but also the hyper-singular operator $\mathcal{H}\{f\}(\mathbf{x}) = \hat{\mathbf{n}}_\mathbf{x} \cdot \nabla D\{f\}(\mathbf{x})$ and the double-layer-adjoint operator $D'\{f\}(\mathbf{x}) = \hat{\mathbf{n}}_\mathbf{x} \cdot \nabla S\{f\}(\mathbf{x})$. Here, $\hat{\mathbf{n}}_\mathbf{x}$ is the surface normal vector at point $\mathbf{x}$, and the gradient here must of course be with respect to $\mathbf{x}$ also. These operators appear in the Burton-Miller formulation [26], which is one approach for addressing the well-known non-uniqueness problem, and when modelling very thin plates [9]. They may be computed by taking the gradient of Ψ_j^D and Ψ_j^S, which in turn involves taking the gradient of (14) and (15). When $\mathbf{x} \notin \partial S_j$, the gradient may be moved inside the contour integral and applied to the kernels in a straightforward way.

The result of this is also implemented in the Matlab toolbox and a direct reference implementation using 2D adaptive quadrature is again also provided. Verification was performed in the same manner as before; error magnitude was below 10^{-7} for $\mathbf{x} \notin S_j$ and below 10^{-5} for $\mathbf{x} \in S_j$. Versions using envelope functions of Peake *et al.* are also included, and the error magnitude between these codes was below 10^{-7} for $\mathbf{x} \notin S_j$.

Numerical integration of the hyper-singular operator $\mathcal{H}$ is notoriously challenging, leading to complicated regularisation procedures such as those described in [7] and [8]. In contrast, the gradient operator was applied to the contour integration formulations of Section 3 without any further regularisation, and it is able to handle the case where $\mathbf{x} \in S_j$ without issue. Terai regularised the hyper-singular operator for piecewise-constant planar elements as a contour integral in [9], and his formulation for computing $\mathcal{H}\{b_j\}(\mathbf{x})$ is equivalent to our method if we choose $\mathbf{k}_j = \pm k\hat{\mathbf{n}}$

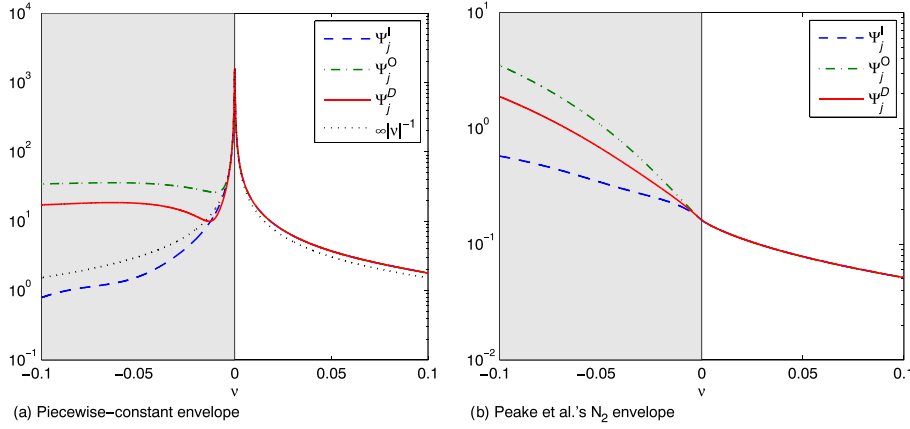Numerical issues do however arise when $\mathbf{x}$ approaches ∂S_j. Plots of $\hat{\mathbf{n}}_j \cdot \nabla \Psi_j^I$, $\hat{\mathbf{n}}_j \cdot \nabla \Psi_j^O$ and $\hat{\mathbf{n}}_j \cdot \nabla \Psi_j^D$ versus the proximity of $\mathbf{x}$ to ∂S_j are shown in Figure 11. Figure 11a considers the case

Figure 11. Plots of $\left|\hat{\mathbf{n}}_j \cdot \nabla \Psi_j^{\mathrm{I}}\right|$, $\left|\hat{\mathbf{n}}_j \cdot \nabla \Psi_j^{\mathrm{O}}\right|$ and $\left|\hat{\mathbf{n}}_j \cdot \nabla \Psi_j^{\mathrm{D}}\right|$ with points $\mathbf{x}$ lying in the plane of S_j (parameters as Figure 10). These are arranged in a line that crosses one edge of S_j; the horizontal coordinate ν states the position of $\mathbf{x}$ relative to the edge (at $\nu = 0$) as a fraction of the element size, and the grey shaded area indicates points on S_j. (a) Depicts the result for piecewise-constant envelope functions, and a singularity can be seen in all variants of $\hat{\mathbf{n}}_j \cdot \nabla \Psi_j$ at $\nu = 0$ due to the discontinuity in the basis function. (b) Depicts the result with the N_2 envelope function of Peake *et al.*; these are continuous, indicating that the values of $\hat{\mathbf{n}}_j \cdot \nabla \Psi_j$ are non-singular.

where a piecewise-constant envelope function was used, and it can be clearly seen that all three quantities are singular as $\mathbf{x}$ crosses ∂S_j. It is unsurprising that issues should occur here, because it is known that use of the hyper-singular operator requires $C^{1,\alpha}$ basis functions, and piecewise-constant elements do not satisfy this (although many collocation codes for thin panels ignore this stipulation). This is discussed in detail by Krishnasamy *et al.* [8], who predicted that the singularity that results from breaking this condition will be $\mathrm{O}(\log |\nu|)$, where ν is the minimum distance from $\mathbf{x}$ to ∂S_j. In Figure 11a, however, it appears to be closer to $\mathrm{O}\left(|\nu|^{-1}\right)$. Examination of the diffracted component of the Ψ_j^{O} in Figure 4b provides a graphical explanation for this. From this, it is clear that the diffracted field is finite close to S_j, but also that there is a variation with angle around the edge, which is roughly independent of distance from the edge; this phenomenon is clearest on the left hand side of Figure 4b. It follows that there is a derivative with respect to angle around that edge and that the component of this contributes to $\hat{\mathbf{n}}_j \cdot \nabla \Psi_j^{\mathrm{O}}$ will be inversely proportional to $|\nu|$, explaining the trend seen in Figure 11a. Equivalent behaviour is seen in line-integral representations of scattering from sound hard wedges (e.g. Equation (4) of [27]).

Related issues regarding the smoothness of basis functions were also encountered by Diwan *et al.* in their study of implementing POU-BEM according to the Burton-Miller formulation [28]. This pertained to the discontinuous derivative, which exists when their N_1 and N_3 envelope functions are joined on neighbouring elements. Their solution for their collocation scheme was simply to avoid this by not picking collocation points on element boundaries. They, however, reported very poor convergence when integrating their Burton-Miller kernels, so this behaviour may go some way towards explaining that. Picking abscissae not on ∂S_j is also not a viable solution for a Galerkin formulation; numerical experiments have shown that the self-interaction double integral of $\hat{\mathbf{n}}_j \cdot \nabla \Psi_j^{\mathrm{D}}$ over an element with a piecewise-constant envelope function diverges as increased quadrature resolution is applied. The situation may be less extreme for basis functions, which are continuous but not smooth, such as joined versions of N_1 and N_3; this has not been investigated. However, it also is possible to form a $C^{1,\alpha}$ discretisation using multiple overlapping copies of the N_2 function of Peake *et al.*, so properties of $\hat{\mathbf{n}}_j \cdot \nabla \Psi_j$ when using that are of great interest. For this case, the behaviour of $\hat{\mathbf{n}}_j \cdot \nabla \Psi_j^{\mathrm{I}}$, $\hat{\mathbf{n}}_j \cdot \nabla \Psi_j^{\mathrm{O}}$ and $\hat{\mathbf{n}}_j \cdot \nabla \Psi_j^{\mathrm{D}}$ for $\mathbf{x}$ near to ∂S_j is plotted in Figure 11b. Here, it can be seen that all three fields are well behaved and finite. The integration methods described herein can therefore also be recommended for computing $\mathcal{H}$ when the basis functions are in $C^{1,\alpha}$. How such a scheme would be used to model a non-smooth obstacle is, however, an open question.

5. CONCLUSIONS AND FURTHER WORK

This paper has presented numerical routines for computing integrals arising in HF-BEM. These operate by transforming surface integrals over elements into contour integrals around the edges of elements. Such contour integral transforms have previously been applied in BEM to regularise the singularities due to the Green's function, and the formulations herein have been shown to address that issue too. In addition, they reduced the computational complexity for computing oscillatory integrals from $O(k^2)$ to $O(k)$, and this has the potential to deliver significant computational cost savings for HF-BEM implementations operating at large values of k.

The contour integral transform was found by identifying an equivalence between a new way of stating HF-BEM discretisation, in terms of incoming and outgoing waves, and existing work on modelling aperture diffraction published within the optics community. Some of this work, particularly the Maggi-Rubinowicz formulation, has been mentioned previously in the BEM literature (e.g. in Section 3.2 of [9]); however, these mentions are only with regard to it being used as an approximate reference solution. Its application to the computation of BEM matrix coefficients is believed to be novel, as is the transformation of oscillatory integrals to contour integrals by this approach.

The contour integral formulation presented places few restrictions on the element shape, although it does require the envelope function present in the basis function be piecewise-constant. The equivalence between the inward and outward wave representation and the more common single and double layer potentials, however, requires that the elements be planar. It was shown that the requirement for piecewise-constant envelope functions can be circumvented if the elements are parallelograms, in which case results for the trigonometric window functions of Peake *et al.* can be computed.

A summary of how the results in this paper might form an integration algorithm for HF-BEM, as implemented in the accompanying Matlab toolbox, is as follows:

- (14) and (15) allow the radiation of a plane wave through an aperture to be computed as a contour integral. This is equivalent to the basis function to point computation defined in (12) when the envelope function is piecewise-constant (10) and the oscillatory function is a plane wave (9). There are no additional limitations on element geometry (beyond what is usual in BEM), though the toolbox only implements these integrals for planar polygonal elements. Use of (15) is preferred in most cases, because it avoids issues associated with the boundary of the geometric visibility zone; however, (14) should be used if the oscillatory function is an evanescent wave and the distance from $\mathbf{x}$ to S_j is significant (in this case $\text{illum}_j(\mathbf{x}) = 0$).
- (19) and (20) allow results from the standard single and double layer potentials to be computed from the aforementioned points. This introduces the additional limitation that the elements must be planar. The envelope functions are still considered to be piecewise-constant.
- Section 4.3 describes how to extend the aforementioned points to the trigonometric envelope functions proposed by Peake *et al.* in [25]. This places the additional limitation that the elements must be parallelograms.

In terms of future work, it has already been mentioned in Section 4.4 that computation of the gradient requires more research. In particular, it was shown that the algorithm can compute results for $C^{1,\alpha}$ basis functions even when the evaluation point lies close to the edge of an element. However, the code currently achieves this by computing weighted sums of other integrals, which themselves are singular; hence, it is extremely inefficient when using an adaptive solver; a more efficient implementation would require all the terms to be combined inside one kernel function.

Other avenues for future development would be to investigate other oscillatory functions and surface geometries. In terms of the contour integral transform, this should just amount to evaluating (17) for other choices of o_j. However, there also needs to be an appropriate transform between the incoming and outgoing wave representation and the double and single layer potentials. The fundamental requirement for this is that the formulae for the incoming and outgoing waves are separable and that one of those component functions is constant over the element. Obvious examples

include cylindrical harmonics used with cylindrical surface sections and spherical harmonics used with spherical surface sections. Because these can be decomposed into trigonometric functions, it seems likely that smooth envelope functions equivalent to those by Peake *et al*. could also be constructed for such schemes.

It would be extremely useful to also be able to efficiently integrate piecewise-polynomial envelope functions, because these are very widely used. Integration with quadratic order polynomials or higher seems unlikely, but should be possible with piecewise-linear functions. The strategy to achieve this would be to consider o_j to be a plane wave multiplied by a linear envelope function e_j, which is constant in the direction in which o_j is propagating. This combination would satisfy $\nabla^2 e_j = 0$ and $\nabla e_j \cdot \nabla o_j = 0$, hence $\nabla^2 (e_j o_j) = -k^2 e_j o_j$, meaning (17) could in principle be used to find an equivalent contour integral kernel. Problems may, however, arise for surface-tangential and evanescent waves, for which it would be difficult to find useful choices of e_j that satisfy $\nabla e_j \cdot \nabla o_j = 0$.

Finally, the most impactful next step may be to apply the method of steepest descent [6] to the contour integrals. This should be relatively straightforward for the polygonal elements considered herein, because the contour integral kernels are extremely similar to those that occur in the Biot-Tolstoy-Medwin expression for diffraction from an infinite rigid wedge, and the method of steepest descent has already been applied to this [29]. This would reduce the computational complexity to be k-independent, which would make this integration approach extremely competitive for HF-BEM methods operating with extremely large k.

APPENDIX A

Having a geometric derivation of a contour integral transform has been stated to be advantageous in the field of aperture diffraction [23], but Asvestas' formulation in section 3.2 is currently lacking one. In what follows, (15) will be derived and explained through considering a new geometric construction, created in such a way so as to eliminate the requirement for a regularising term. This construction differs from those used previously as it only involves a surface integral over the finite cone whose base is the aperture and whose vertex is the observation point, whereas previous constructions have always involved some form of cone of infinite extent (see e.g. Figure 1 of [30] or Figs. 2 and 3 of [23]). The new geometry is depicted in Figure A.1. Two slightly different cases arise; Figure A.1a shows the version when **x** is 'above' S_j, so $\hat{\mathbf{n}} \cdot \mathbf{R} > 0$, and Figure A.1b shows the version when **x** is 'below' S_j, so $\hat{\mathbf{n}} \cdot \mathbf{R} < 0$. The cone has been truncated by subtracting its intersection with a sphere of limitingly-small radius ε centred on **x**; this introduces an additional small spherical cap designated C. With this modification both Φ_j and G satisfy the wave equation

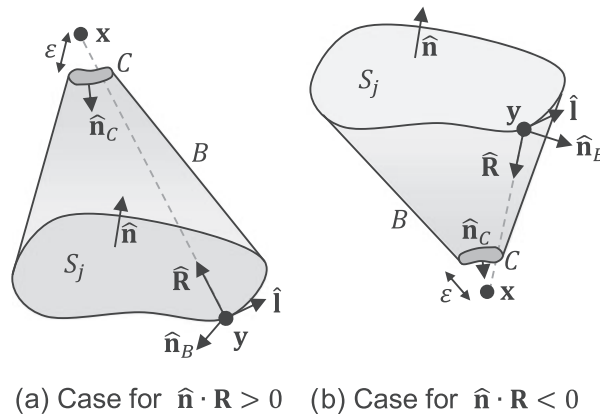(a) Case for $\hat{\mathbf{n}} \cdot \mathbf{R} > 0$ (b) Case for $\hat{\mathbf{n}} \cdot \mathbf{R} < 0$

Figure A.1. Truncated cone construction equivalent to Asvestas' formulation, including the coordinate system used in the Appendix.

everywhere in the region enclosed by S_j, C and the side of the cone B, hence applying Green's second identity over this volume gives:

$$\int\!\!\!\int_{S_j \cup B \cup C} \hat{\mathbf{n}}\,(\mathbf{y}) \cdot \mathbf{I}\,(\mathbf{x},\mathbf{y})\,dS_{\mathbf{y}} = 0. \tag{A.1}$$

Here we have again assumed that $e_j\,(\mathbf{y}) = 1$ for $\mathbf{y} \in S_j$, so $\mathbf{I}\,(\mathbf{x},\mathbf{y}) = o_j\,(\mathbf{y})\,\nabla G\,(\mathbf{x},\mathbf{y}) - G\,(\mathbf{x},\mathbf{y})\,\nabla o_j\,(\mathbf{y})$. It follows therefore that:

$$\Psi_j\,(\mathbf{x}) = -\iint_{B \cup C} \hat{\mathbf{n}}\,(\mathbf{y}) \cdot \mathbf{I}\,(\mathbf{x},\mathbf{y})\,dS_{\mathbf{y}}. \tag{A.2}$$

Note that this relation is only possible because Φ and $\partial\Phi/\partial n$ were discretised together using a basis function which is a wave term o_j multiplied by a piecewise constant window function.

The next step is to convert the surface integral over B into spherical polar coordinates so it can be integrated analytically in one dimension, producing a contour integral. As described in section 2A of [23], the surface integral over B can be restated as a double integral with respect to polar radius r and distance l along the aperture rim. Using this gives $dS = \left|\hat{\mathbf{R}} \times \hat{\mathbf{l}}\right| r/R\,dr\,dl$, which compensates for the fact that $\hat{\mathbf{R}}$ and $\hat{\mathbf{l}}$ may not be completely perpendicular and the radial scaling with r. The normal vector on B is perpendicular to both $\hat{\mathbf{R}}$ and $\hat{\mathbf{l}}$ and may be found by $\hat{\mathbf{n}} = \hat{\mathbf{R}} \times \hat{\mathbf{l}}\,/\left|\hat{\mathbf{R}} \times \hat{\mathbf{l}}\right|$; this applies to both cases in Figure A.1 a and b. Putting these together and taking the limit as $\varepsilon \to 0$ gives:

$$\iint_B \hat{\mathbf{n}}\,(\mathbf{y}) \cdot \mathbf{I}\,(\mathbf{x},\mathbf{y})\,dS_{\mathbf{y}} = \oint_{S_j} \lim_{\varepsilon \to 0} \int_\varepsilon^R \frac{r}{R}\hat{\mathbf{R}} \times \hat{\mathbf{l}}\,(\mathbf{y}) \cdot \mathbf{I}\left(\mathbf{x}, \mathbf{x} - r\hat{\mathbf{R}}\right)dr\,dl_{\mathbf{y}} = -\oint_{S_j} \hat{\mathbf{l}}\,(\mathbf{y}) \cdot \mathbf{J}\,(\mathbf{x},\mathbf{y})\,dl_{\mathbf{y}}. \tag{A.3}$$

Considering the form of the inner integral demonstrates why $\mathbf{J}$ may be found from $\mathbf{I}$ by (17).

For the cap of the cone a procedure is followed which is equivalent to what is used in the derivation of the Kirchhoff-Helmholtz integral equation to bring the pressure at $\mathbf{x}$ onto the left hand side. The definition of C gives that $R = \varepsilon$ and $\hat{\mathbf{n}} = s_n\hat{\mathbf{R}}$, where s_n is a parameter which is defined to equal -1 for the case in Figure A.1a and $+1$ for the case in Figure A.1b. The integrand may be expanded as $\hat{\mathbf{n}} \cdot \mathbf{I}\,(\mathbf{x},\mathbf{y}) = s_n o_j\,(\mathbf{y})\,\hat{\mathbf{R}} \cdot \nabla G\,(\mathbf{x},\mathbf{y}) - s_n G\,(\mathbf{x},\mathbf{y})\,\hat{\mathbf{R}} \cdot \nabla o_j\,(\mathbf{y})$. Considering the second term, since $\left|\nabla o_j\,(\mathbf{y})\right|$ is bounded in the neighbourhood of $\mathbf{x}$ and $\left|\nabla o_j\,(\mathbf{y}) \cdot \hat{\mathbf{R}}\right| \le \left|\nabla o_j\,(\mathbf{y})\right|$, it follows that the integral of $\hat{\mathbf{R}} \cdot \nabla o_j\,(\mathbf{y})$ over C is $O\left(\varepsilon^2\right)$ and the term $G\,(\mathbf{x},\mathbf{y})\,\hat{\mathbf{R}} \cdot \nabla o_j\,(\mathbf{y})$ tends to zero as $\varepsilon \to 0$. In the first term, G is constant over C because it is spherical and $o_j\,(\mathbf{y})$ may be approximated by $o_j\,(\mathbf{x})$ since C is vanishingly small. Substituting all this and $\hat{\mathbf{R}} \cdot \nabla G = -\partial G/\partial R = -G\,[ik - 1/R]$ gives:

$$\begin{aligned}
\lim_{\varepsilon \to 0} \iint_C \hat{\mathbf{n}}\,(\mathbf{y}) \cdot \mathbf{I}\,(\mathbf{x},\mathbf{y})\,dS_{\mathbf{y}} &= s_n \lim_{\varepsilon \to 0} \iint_C o_j\,(\mathbf{y})\,\hat{\mathbf{R}} \cdot \nabla G\,(\mathbf{x},\mathbf{y})\,dS_{\mathbf{y}} \\
&= s_n o_j\,(\mathbf{x}) \lim_{\varepsilon \to 0} \left[\frac{e^{ik\varepsilon}}{4\pi\varepsilon}\left[\frac{1}{\varepsilon} - ik\right]\iint_C dS\right] \\
&= o_j\,(\mathbf{x})\frac{\Omega_C\,(\mathbf{x})}{4\pi}\lim_{\varepsilon \to 0}\left[e^{ik\varepsilon}\,[1 - ik\varepsilon]\right] \\
&= o_j\,(\mathbf{x})\frac{\Omega_C\,(\mathbf{x})}{4\pi}.
\end{aligned} \tag{A.4}$$

Here $\Omega_C\,(\mathbf{x})$ is the solid angle at $\mathbf{x}$ subtended by the domain C. Note that orientation of $\hat{\mathbf{n}}$ with respect to the radial vector $\hat{\mathbf{R}}$ affects the sign of Ω_C (it is negative if they point in opposite directions),

hence the term s_n has been absorbed into Ω_C. Observing the geometry it is obvious that Ω_C is equal to the solid angle $\Omega_{S_j}(\mathbf{x})$ subtended by S_j but with a change of sign; $\Omega_C(\mathbf{x}) = -\Omega_{S_j}(\mathbf{x})$. Substituting this and (A.3) and (A.4) into (A.2) produces (15) as derived by Asvestas.

REFERENCES

1. Gumerov N, Duraiswami R. *Fast Multipole Methods for the Helmholtz Equation in Three Dimensions*. Elsevier Science: Oxford, 2005. 426 pages.
2. Perrey-Debain E, Laghrouche O, Bettess P, Trevelyan J. Plane-wave basis finite elements and boundary elements for three-dimensional wave scattering. *Philosophical Transactions of the Royal Society of London Series A* 2008; **362**:561–577. DOI: 10.1098/rsta.2003.1335.
3. Chandler-Wilde SN, Graham IG, Langdon S, Spence EA. Numerical-asymptotic boundary integral methods in high-frequency acoustic scattering. *Acta Numerica* 2012; **21**:89–305. DOI: 10.1017/S0962492912000037.
4. Trevelyan J, Honnor ME. A numerical coordinate transformation for efficient evaluation of oscillatory integrals over wave boundary integrals. *Journal of Integral Equations and Applications* 2009; **21**(3):449–470. DOI: 10.1216/JIE-2009-21-3-449.
5. Bruno OP, Geuzaine CA. An o(1) integration scheme for three-dimensional surface scattering problems. *Journal of Computational and Applied Mathematics* 2007; **204**(2):463–476.
6. Huybrechs D, Vandewalle S. On the evaluation of highly oscillatory integrals by analytic continuation. *SIAM Journal on Numerical Analysis* 2006; **44**(3):1026–1048.
7. Chien CC, Rajiyah H, Atluri SN. An effective method for solving the hyper-singular integral equations in 3-D acoustics. *Journal of the Acoustical Society of America* 1990; **88**(2):918–937.
8. Krishnasamy G, Schmerr LW, Rudolphi TJ, Rizzo FJ. Hypersingular boundary integral equations: some applications in acoustic and elastic wave scattering. *Journal of Applied Mechanics* 1990; **57**(2):404–414.
9. Terai T. On calculation of sound fields around three dimensional objects by integral equation methods. *Journal of Sound and Vibration* 1980; **69**(1):71–100.
10. Wu H, Liu Y, Jiang W. A low-frequency fast multipole boundary element method based on analytical integration of the hypersingular integral for 3D acoustic problems. *Engineering Analysis with Boundary Elements* 2013; **37**(2):309–318.
11. Asvestas JS. Line integrals and physical optics. Part II. The conversion of the Kirchhoff surface integral to a line integral. *Journal of the Optical Society of America A* 1985; **2**(6):896–902.
12. Gordon W. Far-field approximations to the Kirchoff-Helmholtz representations of scattered fields. *IEEE Transactions on Antennas and Propagation* 1975; **23**:590–592.
13. Gabard G. Exact integration of polynomial-exponential products with application to wave-based numerical methods. *Communications in Numerical Methods in Engineering* 2009; **25**:237–246.
14. Cox TJ, D'Antonio P. *Acoustic Absorbers and Diffusers*. Taylor & Francis: London, 2009. 432 pages.
15. Hargreaves JA, Lam YW. Time domain modelling of room acoustics. *Proceedings of the Institute of Acoustics*, 2012.
16. Hargreaves JA, Lam YW. Towards a full-bandwidth numerical acoustic model. *Proceedings of Meetings on Acoustics* 2013; **19**:015096. DOI: 10.1121/1.4800226.
17. Hargreaves JA, Cox TJ. A transient boundary element method model of Schroeder diffuser scattering using well mouth impedance. *Journal of the Acoustical Society of America* 2008; **124**(5):2942–2951.
18. Hewett DP, Langdon S, Chandler-Wilde SN. A frequency-independent boundary element method for scattering by two-dimensional screens and apertures. *IMA Journal of Numerical Analysis* 2015; **35**(4):1098–1728.
19. Miyamoto K, Wolf E. Generalization of the Maggi-Rubinowicz Theory of the boundary diffraction wave - Part I. *Journal of the Optical Society of America* 1962; **52**(6):615–625.
20. Asvestas JS. Line integrals and physical optics. Part I. The transformation of the solid-angle surface integral to a line integral. *Journal of the Optical Society of America A* 1985; **2**(6):891–895.
21. Guiggiani M. The evaluation of cauchy principal value integrals in the boundary element method—a review. *Mathematical and Computer Modelling* 1991; **15**(3):175–184.
22. Guiggiani M, Krishnasamy G, Rudolphi TJ, Rizzo FJ. A general algorithm for the numerical solution of hypersingular boundary integral equations. *Journal of Applied Mechanics* 1992; **59**(3):604–614.
23. Albani M. Boundary diffracted wave and incremental geometrical optics: a numerically efficient and physically appealing line-integral representation of radiation integrals. aperture scalar case. *IEEE Transactions on Antennas and Propagation* 2011; **59**(2):586–594.
24. Melenk JM, Babuška I. The partition of unity finite element method: basic theory and applications. *Computer Methods in Applied Mechanics and Engineering* 1996; **139**(1–4):289–314.

25. Peake MJ, Trevelyan J, Coates G. Novel basis functions for the partition of unity boundary element method for Helmholtz problems. *Internationl Journal for Numerical Methods in Engineering* 2013; **93**(9):905–918.
26. Burton AJ, Miller GF. The application of integral equation methods to the numerical solution of some exterior boundary-value problems. *Philosophical transactions of the Royal Society of London Series A* 1971; **323**(1553): 201–210.
27. Hewett DP, Svensson UP. The diffracted field and its gradient near the edge of a thin screen. *Journal of the Acoustical Society of America* 2013; **134**(6):4303–4306.
28. Diwan GC, Trevelyan J, Coates G. A comparison of techniques for overcoming non-uniqueness of boundary integral equations for the collocation partition of unity method in two-dimensional acoustic scattering. *International Journal for Numerical Methods in Engineering* 2013; **96**(10):645–664.
29. Asheim A, Svensson UP. Efficient evaluation of edge diffraction integrals using the numerical method of steepest descent. *Journal of the Acoustical Society of America* 2010; **128**(4):1590–1597.
30. Rubinowicz A. Geometric derivation of the Miyamoto-Wolf formula for the vector potential associated with a solution of the Helmholtz equation. *Journal of the Optical Society of America* 1962; **52**(6):717–718.

SUPPORTING INFORMATION

Additional supporting information may be found in the online version of this article at the publisher's web site.